


# Atmospheric icing meteorological parameter study using field experiments and simulation

Xingbo Han<sup>1</sup>  | Muhammad Virk<sup>1</sup> | Hamza Asif<sup>1</sup> | Anssi Mäkynen<sup>2</sup> | Harri Juttula<sup>3</sup> | Eero Molkoselkä<sup>2</sup> | Ville A. Kaikkonen<sup>3</sup>

<sup>1</sup>Arctic Technology & Icing Group, UiT-The Arctic University of Norway, Narvik, Norway

<sup>2</sup>Optoelectronics and Measurement Techniques Research Unit, University of Oulu, Oulu, Finland

<sup>3</sup>Unit of Measurement Technology, University of Oulu, Oulu, Finland

## Correspondence

Xingbo Han, Arctic Technology & Icing Group, UiT- The Arctic University of Norway, Narvik, Norway.

Email: [xingbo.han@uit.no](mailto:xingbo.han@uit.no)

## Funding information

the nICE project of UiT & Research Council of Norway, Grant/Award Number: 324156

## Abstract

Atmospheric icing on ground structures is a concern from design, operation, and safety perspectives. Supercooled water droplets size and liquid water content (LWC) are important weather parameters to better understand the ice accretion physics on ground structures. Most existing studies are based on measurements at high altitude. The study is based on the field results of a specific event (from 9:30 to 22:27 h on October 29, 2022) in Arctic region of northern Norway. The data from this event are presented and used for analytical validation and simulation. Field measurements of different meteorological weather parameters including the droplet size and LWC are carried out leading to recording of resultant atmospheric ice load and intensity. A comprehensive study is also carried out to validate droplet collision efficiency and ice load using the existing analytical model ISO-12494 and computational fluid dynamics (CFD)-based numerical simulations. Furthermore, the differences in icing simulation using parameters such as median volume diameter (MVD), Langmuir B -J as alternatives to the actual droplet size distribution (DSD) spectrum are also analyzed. The results show that under natural meteorological conditions, the characteristics of water DSD change in real time. Using MVD alone to calculate the water droplet collision efficiency on circular cylinders can lead to significant errors. Accurately selecting the Langmuir distribution as a substitute for the actual DSD can reduce simulation errors to within 5%. Compared to the analytical model, the numerical simulations result better reflects the collision characteristics of water droplets of different sizes on the cylindrical object.

## KEYWORDS

CFD, droplet size distribution, field measurements, in-cloud icing, ISO-12494, supercooled water droplets

This is an open access article under the terms of the [Creative Commons Attribution](https://creativecommons.org/licenses/by/4.0/) License, which permits use, distribution and reproduction in any medium, provided the original work is properly cited.

© 2024 The Author(s). *Meteorological Applications* published by John Wiley & Sons Ltd on behalf of Royal Meteorological Society.

## 1 | INTRODUCTION

In cold climate regions around the globe, icing on structures is a safety hazard for many industries. For example, power transmission line icing can cause an increase in line load, wire torsion and fracture, insulator ice flash-over discharge, tower collapse, etc. (Shu et al., 2014), resulting in large-scale power outages and huge economic losses. Since the recording of power line icing disasters in 1954, there have been various types of transmission line icing accidents (Hu et al., 2016). Relevant reports have been made in regions such as China (Lei et al., 2016), Canada (Volat et al., 2011), Japan (Matsuda et al., 1991), Norway, Sweden, and the United States (Charneski et al., 1982). In order to study the physics of ice accretion and propose corresponding mitigation methods, extensive research has been conducted. The ice accretion process on structures is relatively complex, with different icing types. The environmental and geometric factors such as the size and shape of the structure, wind speed, temperature, liquid water content (LWC), and water droplet size distribution (DSD) in the air (Jiang et al., 2014) affect the ice accretion process. To quantitatively analyze the icing process and propose corresponding physical and mathematical models, artificial icing experiments in labs or computer-based numerical simulations are usually being used in the research, but not much research work has been carried out in terms of field experimentation in natural conditions.

Improved understanding of ice accretion physics requires knowledge about environmental weather parameters such as wind speed, temperature, relative humidity (RH), water droplet size, and LWC. The measurements of these weather parameters in icing environment are challenging, as even measurement of wind speed requires specially designed heated anemometer. The existing research work about droplet size and LWC measurement has been carried out at higher altitudes with specific focus of aviation sector, and not much work has been done for ground structural icing, and there is also a lack of long-term effective data collection specifically addressing liquid size and LWC under icing conditions (Brun & Mergler, 1953; Goldberg et al., 2018). This makes the applicability of existing analytical model applications for ground structural icing calculation with limited accuracy.

The methods for measuring water DSDs in the atmosphere vary significantly, and their applications differ accordingly. Lawson and Blyth (1998). introduced the use of a cloud droplet spectrometer (CDS) instrument to measure LWC and DSDs at high altitudes (within the isothermal region at altitudes of 0.5 to 2 km). They compared the in-flight measurement data with data from other sensors, including the Forward Scattering Spectral Probe

(FSSP) from Particle Measuring Systems (PMS), the “fast” FSSP (FFSSP) developed by the French National Meteorological Research Centre (CNRM), and Gerber Scientific's Airborne Particle Volume Monitor (PVM.100A), and found good agreement between the results. Subsequent research by Burnet and Brenguier (1999) and others compared the advantages and disadvantages of various methods, such as the Forward Scattering Spectrometer Probe (FSSP), the Fast-FSSP, the CDS, the Particulate Volume Monitor (PVM), the CSIRO hot wire probe, and the Phase Doppler Particle Analyzer (Chuang et al., 2008). But these comparisons were primarily focused on measurements of liquid water at high altitudes. Wang et al. (2023). utilized a dual-channel airborne microwave radiometer to detect supercooled water in cloud layers and developed a supercooled water detection algorithm to address the limitations of other instruments, such as hot-wire LWC sensors, when detecting supercooled water. The research by Inoue and Sato (2023). focused on a novel laser ceilometer with depolarization capability (Vaisala CL61), which was used to distinguish different phases of cloud layers and compare its detection results with a CPS sounding instrument. SEA is also a modern hot-wire device used for LWC measurements, but due to the influence of baseline drift and droplet retention characteristics, its performance calibration still faces some challenges. Guo et al. (2023). developed an in situ drying power calibration method to improve the calibration performance of this sensor. Spirig et al. (2021)., in their study of fog events in Central Namib desert, used a CDP (CDP-2, Droplet Measurement Technologies) to measure water DSD and derive LWC in the air. However, measuring LWC and droplet size on the ground is influenced by wind speed and rainfall, and the LWC obtained with this device is often underestimated when wind speeds are low. Dhar et al (2024 and Dhar and Khawaja 2021)., while investigating ship icing issues, proposed using a laser radar to measure fog droplet impact flux on the ship's surface, but did not provide a detailed description of the DSD. Dai et al (Dai et al., 2022). used an active humidity-controlled aerosol particle sizer to measure aerosol liquid water content (ALWC) in the air at different RH levels, but this device cannot be directly used under icing conditions. Unlike measuring LWC in the air that leads to icing, Gui et al. (2022). discussed and tested a cascade detection method using impedance spectrum characteristics, which can be directly used to measure ice thickness on structures under mixed ice-water conditions. Ge et al. (2022). proposed a fiber-optic sensor-based method for measuring ice accretion thickness and type with a 92.8% accuracy in ice type identification and a 0.27-mm ice thickness measurement error.

According to the standard document ISO 12494 (ISO 12494:2001(E), 2001), both numerical and analytical models for icing calculations require inputs such as LWC and DSD in the air. These inputs are used to calculate the droplet collision efficiency  $\alpha_1$ , sticking efficiency  $\alpha_2$ , and freezing efficiency  $\alpha_3$ . In the simulation of rime ice accretion, the impact of DSD on  $\alpha_1$  is particularly significant. Therefore, when environmental conditions change, it is important to accurately measure and use the MVD or DSD spectrum, which requires further knowledge. There is a lack of sensors for measuring MVD and LWC under severe near-surface icing conditions. The rotating multi-cylinder method (Knezevicil & Kindf, 2014) is commonly used to indirectly measure LWC and the MVD in the air near the ground surface under icing conditions. This method involves measuring the differences in icing rates on various cylinders of different diameters. However, experimental results indicate that as icing time increases, the final diameters of different diameter cylinders tend to be the same. Therefore, it is necessary to ensure that there are always differences in cylinder diameters, and the sensor measurement accuracy should be sufficient to capture the differences in icing rates between the cylinders. In addition, holographic imaging technology is also employed for measuring MVD and LWC (Kaikkonen et al., 2020; Tiitta et al., 2022), such as pioneering work done by Silverman and Thompson (1964), and modern digital holographic airborne cloud measurement system realized by Fugal et al. (2004), but this method also requires heating equipment to ensure that the measurement device is not affected by icing.

Currently, there are two main methods for validating analytical, numerical, and experimental models: artificial and natural icing tests. Artificial icing tests are widely used because they offer controlled conditions. For example, Sokolov and Virk (2019) and Zhang et al. (2017) used wind tunnel icing tests to validate icing models for cylinders. In natural conditions, environmental parameters change in real time, making data collection more challenging. Typically, only icing form and mass are used as validation parameters. For instance, Shu et al (Shu et al., 2018). conducted continuous observations of wind turbine blade icing forms in natural conditions, validating their numerical icing calculation model for wind turbine blades.

This paper focus on field measurements of icing events and validating the existing analytical and numerical models of ice accretion with the experimental data. Circular cylinder is used as reference ice collector. The droplet distribution spectrum and resultant ice accretion loads from field measurements are used for validation with the existing models. The differences in droplet collision characteristics under different DSD and MVD were

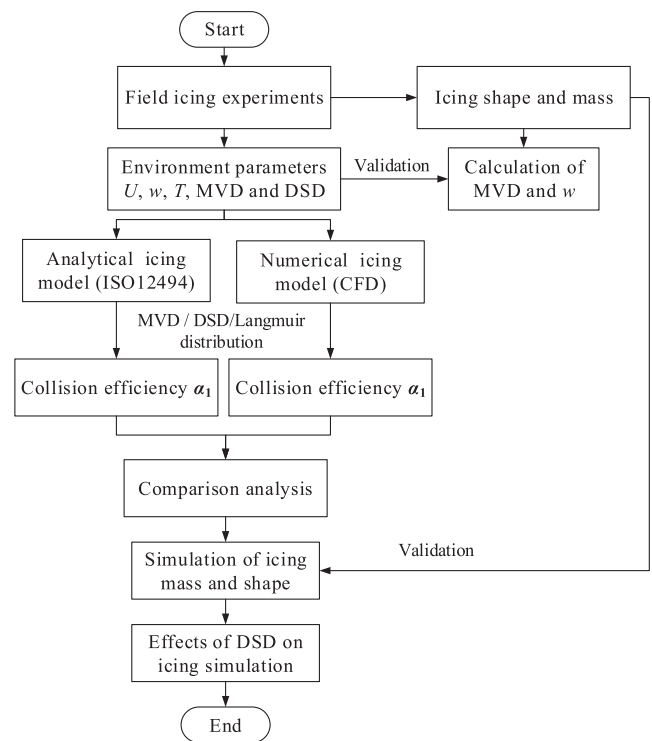


FIGURE 1 Flow chart explaining the analysis procedure used.

analyzed and compared. The aim is to reveal the influence of water DSD under natural conditions on the icing process and to provide technical and data references for precise icing simulation and prediction of cylindrical structures such as transmission lines.

## 2 | DESIGN OF EXPERIMENTS

In this study, the results from analytical, numerical, and field experiments are used. Main focus has been on the field measurements of meteorological icing parameters in natural conditions and then use the existing analytical (ISO12494) model and multiphase CFD-based numerical models to validate with the field measurements. Using analytical and numerical models, this study calculates droplet collision coefficients on the surface of a cylinder under three different conditions: MVD, DSD, and Langmuir DSDs. The input data for these calculations are obtained from water DSDs and MVD collected by ICEMET sensor (Juttula et al., 2022; Molkoselka et al., 2021) installed in the field. Additionally, simulated calculations are performed to replicate the ice accretion morphology and thickness on the cylinder surface. These simulations are then validated against real field measurement data. This approach enables a more comprehensive analysis of the impact of DSD characteristics on ice accretion simulations, as depicted in the specific framework presented in Figure 1.

## 2.1 | Field experiment setup

The field icing experiments were carried out at 1000 m above sea level at 68 degree north in the arctic circle of norther Norway. This station is installed by UiT researchers. A state-of-the-art field ice monitoring station comprises various meteorological sensors, and icing sensors are used. Wind speed, wind direction, atmospheric temperature, RH, and pressure are measured using a heated multipurpose weather sensor. LWC and droplet size measurements are carried out using ICEMET sensor. Accreted ice load and icing intensity are measured using two ice load monitors (IL1 and IL2) and T-44 HoloOptic sensor. Additional ICETROLL sensor is installed for comparison of ice load from ice load monitors. A video camera with heated lenses is installed to monitor the icing event. Figure 2 shows the field ice monitoring station used in this study.

To comprehensively demonstrate the differences between MVD (Lang-A, monodisperse distribution) and DSD for simulating icing, field icing experiments on two

circular cylinder-based icing sensors are carried out. Both sensors have different cylinder diameters, where IL-1 has 30 mm cylinder diameter, whereas IL-2 has 57 mm diameter cylinder rod 0.5-m length. Due to the high altitude of the test site, strong winds, and proximity to water sources, icing is very severe in winter. As shown in Figure 3, the icing test tower was completely covered by ice, forming a thick wing-shaped ice cover on the windward side of the cylinders.

## 2.2 | Analytical model

To estimate the droplet collision from accreted ice load, ISO-12494-based analytical modelling approach is used in this study. Ice accretes due to particles in the air colliding with the object. These particles can be liquid (usually super-cooled), solid, or a mixture of water and ice. In any case, the maximum rate of icing per unit projection area of the object is determined by the flux density of these particles. The flux density,  $dm/dt$  (kg/s), is a product of

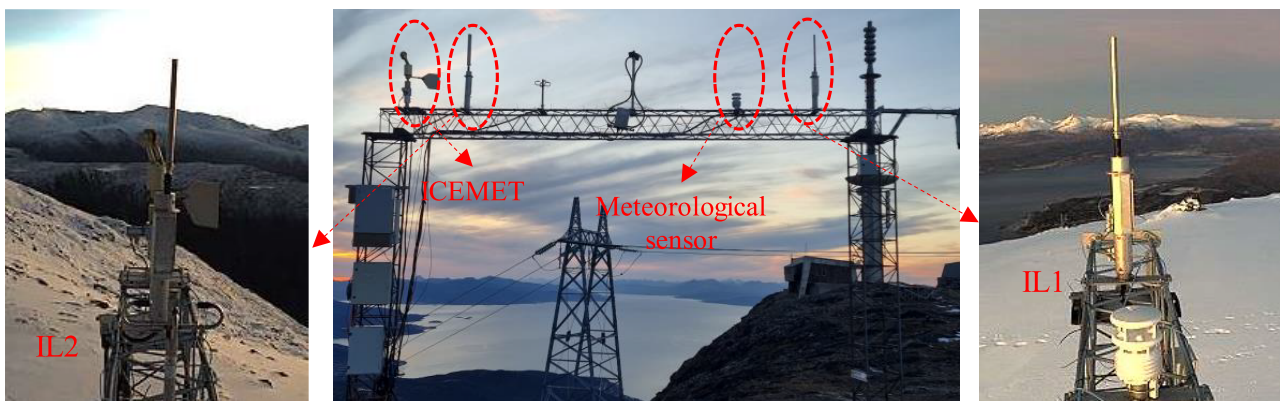


FIGURE 2 Field ice monitoring station setup.



FIGURE 3 Field icing station during winter season.



the mass concentration of the particles,  $w$  (LWC, water liquid content in the air,  $\text{kg}/\text{m}^3$ ), and the velocity,  $U$  (m/s), of the particles with respect to the object. Consequently, the rate of icing is obtained from Equation (1).

$$\frac{dm}{dt} = \alpha_1 \alpha_2 \alpha_3 \cdot w \cdot A \cdot U \quad (1)$$

where  $A$  is the cross-sectional area of the object, square meter. If a single size water droplet diameter spectrum, MVD (Lang-A), is used instead of the DSD, then as per the Finstad icing model of 1988, the collision coefficient of water droplets on a cylinder  $\alpha_1$  can be calculated according to the formula (Finstad et al., 1988) in Equation (2).

$$\alpha_1(K, \phi) = \left[ C_{x1} K^{C_{x2}} e^{(C_{x3} K^{C_{x4}})} + C_{x5} \right] - \left[ C_{x6} (\phi - 100)^{C_{x7}} \right] \\ \times \left[ C_{x8} K^{C_{x9}} e^{(C_{x10} K^{C_{x11}})} + C_{x12} \right] \quad (2)$$

where  $C_{x1}$ – $C_{x12}$  are constant coefficients and  $K$  and  $\phi$  represent the inertia parameter and Langmuir parameter during the movement of water droplets, respectively:

$$K = \frac{\text{MVD}^2 \rho_d U_0}{9\mu D} \quad (3)$$

$$\phi = \frac{18\rho_a^2 D U_0}{\rho_d \mu} \quad (4)$$

where  $\rho_d$  and  $\rho_a$  are the density of water droplets and air, respectively,  $\text{kg}/\text{m}^3$ ;  $U_0$  is the wind speed, m/s;  $D$  represents the diameter of the cylinder (or the cylinder covered with ice), m;  $\mu$  is the kinematic viscosity of air,  $\text{m}^2/\text{s}$ . In addition, when the constant coefficients  $C_{x1}$ – $C_{x12}$  take different values,  $\alpha_1$  can also represent the local droplet collision coefficient  $\beta_0$  at the centre line of a cylinder, maximum collision angle  $\alpha_0$  (rad), and droplet collision velocity  $V_0$  (dimensionless), the detail values of  $C_{x1}$ – $C_{x12}$  can be found in the reference (Finstad et al., 1988). If the DSD spectrum is used to calculate the droplet collision coefficient on a cylinder, the diameter of droplets in the air is divided into  $n$  intervals, the average value of droplet diameter in each interval is  $d_i$ , and the volume fraction is  $P_i$ . The collision coefficient of water droplets with a diameter of  $d_i$  on the cylinder is  $E(d_i)$ ; then, the overall droplet collision coefficient is  $\alpha_1$  which is calculated as:

$$\alpha_1 = \sum_{i=1}^n P_i E(d_i) \quad (5)$$

## 2.3 | Numerical model

The multiphase CFD-based numerical simulations are carried out using Eulerian water droplet impingement solver. The general Eulerian two-phase model for viscous flow consists of the Navier–Stokes equations augmented by the droplet's continuity and momentum equations (FENSAP User Manual ANSYS, 2021):

$$\frac{\partial P_d}{\partial t} + \nabla \cdot (P_d \mathbf{V}_d) = 0 \quad (6)$$

$$\frac{\partial (P_d \mathbf{V}_d)}{\partial t} + \nabla \cdot [P_d \mathbf{V}_d \otimes \mathbf{V}_d] = \frac{C_D \text{Re}_d}{24K} P_d (\mathbf{V}_a - \mathbf{V}_d) \quad (7) \\ + P_d \left( 1 - \frac{\rho_a}{\rho_d} \right) \frac{1}{\text{Fr}^2}$$

where  $P_d$  is the volume fraction of water droplets in the air;  $V_a$  and  $V_d$  are the velocities of air and water droplets, respectively, meter per second;  $C_D$  is the resistance coefficient of water droplets;  $\text{Re}_d$  is the Reynolds number of the water droplet; and  $\text{Fr}$  is the local Froude number (Sokolov & Virk, 2019). According to the basic idea of the Euler method, the local droplet collision coefficient  $\beta_1$  on a cylinder is:

$$\beta_1 = - \frac{P_d \mathbf{V}_d \cdot \mathbf{n}}{w V_\infty} \quad (8)$$

where  $w$  is the LWC in the air, kilogram per cubic meter;  $N$  is the normal vector of the cylinder surface;  $V_\infty$  is the airflow velocity, meter per second. The overall water droplet collision coefficient of a cylinder  $\alpha_1$  is:

$$\alpha_1 = \frac{\int_{C_s} \beta_1 dS}{D \times L} \quad (9)$$

where  $L$  is the length of the cylinder, meter;  $C_s$  is the area of the water droplet collision area on the cylinder, square meter. The icing density on cylinders is calculated according to the following formula:

$$\rho_i = 378 + 425 \log_{10}(R_m) - 82.3 (\log_{10}(R_m))^2 \quad (10)$$

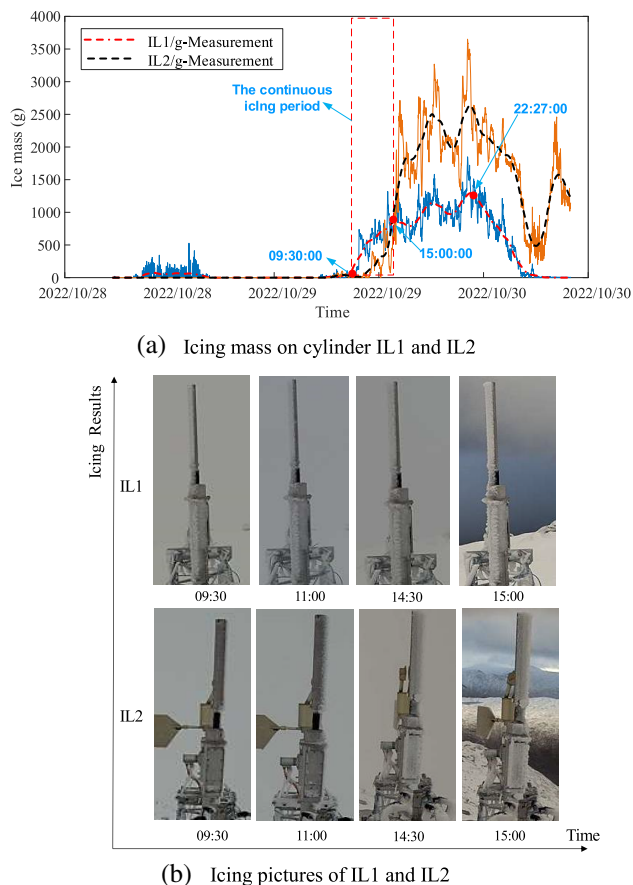


**FIGURE 4** Cylinder icing weight and images. (a) Icing mass on cylinder IL1 and IL2. (b) Icing pictures of IL1 and IL2.

where  $R_m$  is the Macklin density parameter, which is expressed as:

$$R_m = -\frac{V_0 MVD}{2T_s} \quad (11)$$

where  $V_0$  is the impact velocity of the droplet in m/s calculated using Equation (2) and  $T_s$  is the surface temperature.

### 3 | RESULTS AND DISCUSSION

#### 3.1 | Field measurement data

Ice loads in the field are measured using two circular cylinders-based icing sensors. These sensors (*COMBI-TECH Ice load monitors*) were circular cylinders having different diameters (30, 57 mm). The ice load data from sensor with 30 mm cylinder diameter is presented at IL1, whereas ice load data from sensor with 57 mm cylinder diameter is presented at IL2. The purpose of using two different cylinder diameters is to estimate the MVD and

LWC from ice load values using ISO-12494 model. For direct measurements of droplet size DSD and LWC, ICEMET sensor was used and the ICEMET results were calculated using the ICEMET-server version 1.12 with a sampling rate  $0.15 \text{ cm}^3/\text{s}$ ; the calibration and related technical parameters of ICEMET can be referred to in the work of Kaikkonen Ville A and his colleagues (Juttula et al., 2022; Molkoselka et al., 2021). For this study, an icing event occurred on October 29th, 2022 is analyzed. Results show that ice gradually accumulated on the windward side of the ice sensors cylinders. As shown in Figure 4a, taking IL1 as an example, the accreted ice mass on cylinder IL1 began to increase from 9:30 h, and gradually grew until it reached its maximum value at 22:27 h. However, during the period from 15:00 to 22:27, there is a brief decrease in ice mass followed by an increase. This phenomenon is likely due to the influence of the wind, resulting in both icing and ice shedding. As shown in Figure 4b, the ice accumulated on the windward side of the cylinders and the ice thickness gradually increased.

As shown in Figure 5a–e, during this icing period, environmental weather parameters such as wind speeds varied between 5.0 and 15.0 m/s, the environmental temperature ranged from  $-2$  to  $-4^\circ\text{C}$ , RH fluctuated between 92.0% and 96.5%, the median volume diameter (MVD) of water droplets ranged from 9 to  $49.7 \mu\text{m}$ , and LWC ranged from 0.03 to  $0.6 \text{ g}/\text{m}^3$ . It is worth noting that the ambient temperature dropped below  $0^\circ\text{C}$  as early as 4:48 h on this day. However, it was not until 9:30 that the surface icing mass on the cylinder began to significantly increase. The reason for the initial lack of ice accretion on cylinders may be twofold: (1) The surface of IL1 and IL2 may not have cooled down to below  $0^\circ\text{C}$ . (2) Although the LWC is not small, the wind speed is low, and the speed and quantity of water droplets colliding with the cylinder with the wind are relatively small. After 9:30, the wind speed and LWC increased significantly ( $U > 6 \text{ m/s}$ ), ultimately leading to the icing event.

As shown in Figure 5a,b, the results for MVD and LWC revealed that when there was no icing, the LWC in the air was extremely low, typically below  $0.03 \text{ g}/\text{m}^3$ . In contrast, during the icing period, LWC was mostly above  $0.2 \text{ g}/\text{m}^3$ . Correspondingly, while during the icing period, MVD was typically above  $20 \mu\text{m}$ . The DSD in the air changed in real time during the icing period. If we consider 30-min intervals for statistical analysis, the DSD spectrum can be obtained. The dispersion of droplet sizes can be expressed by the standard deviation ( $\sigma$ ).

$$\sigma = \sum_{i=1}^{10} P_i \times (d_i - \text{MVD})^2 \quad (12)$$

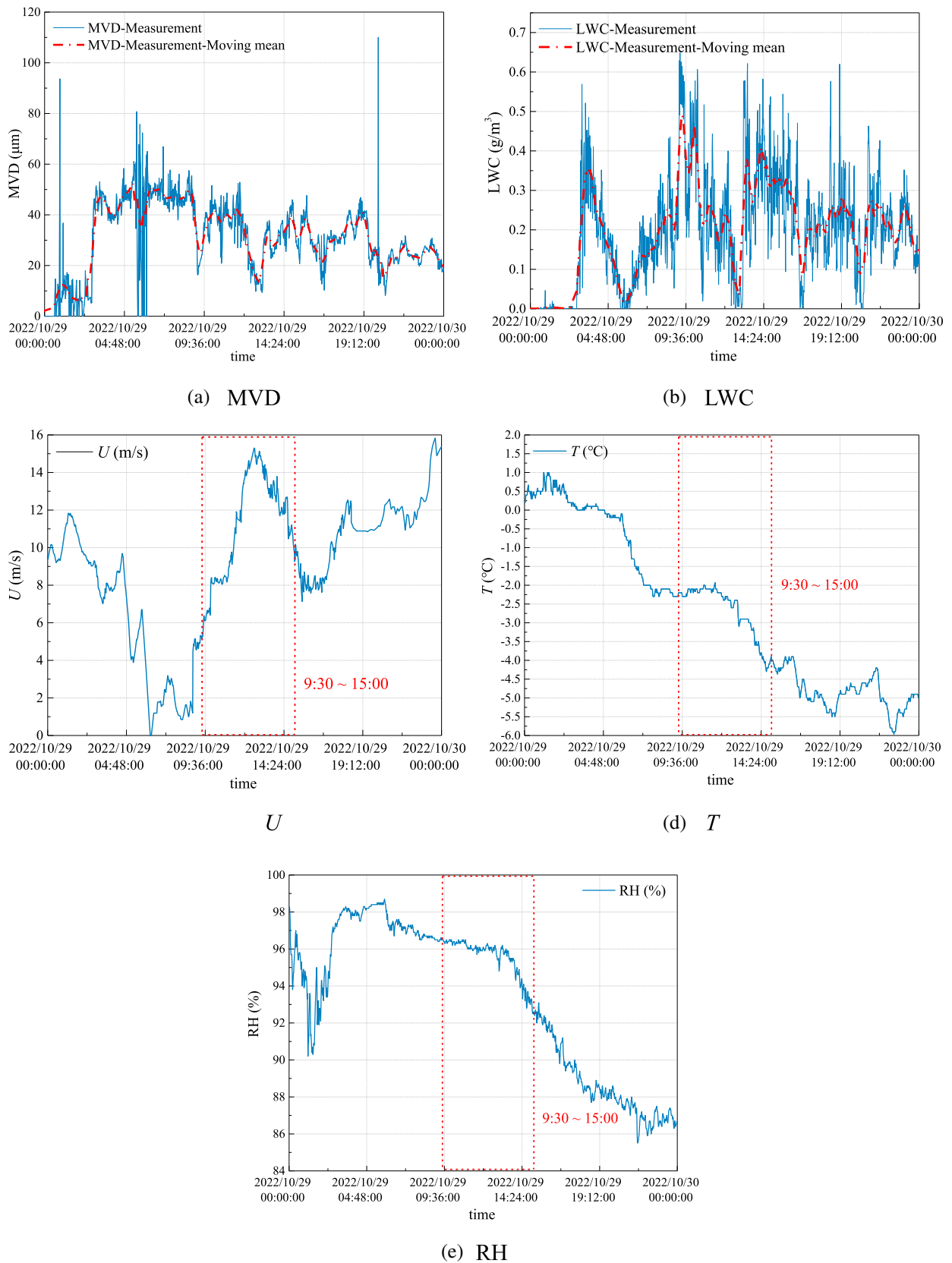


**FIGURE 5** Environmental weather parameters during the icing event. (a) MVD. (b) LWC. (c)  $U$ . (d)  $T$ . (e) RH. LWC, liquid water content; MVD, median volume diameter; RH, relative humidity.

where  $d_i$  represents the droplet diameter. Table 2 presents the droplet distribution spectrum. To reduce computational complexity, when  $5 \mu\text{m} \leq d_i < 10 \mu\text{m}$ ,  $d_i$  is taken as  $7.5 \mu\text{m}$ , and so on, resulting in  $d_i$  of  $7.5, 12.5, 17.5 \mu\text{m}$ , and so forth.  $P_i$  is the volume fraction of droplets with diameters ranging from  $d_i - 2.5 \mu\text{m}$  to  $d_i + 2.5 \mu\text{m}$  within the total volume of all droplets.

Between 9:30 and 22:27 h on October 29, 2022, this time frame was divided into 11 intervals. The MVD of water droplets during this period ranged from 17 to  $39 \mu\text{m}$ . As shown in Figure 6, by extracting the volume fractions of different-sized droplets within each of the 11 intervals, a water DSD spectrum can be plotted. Over these 11 intervals, the standard deviation of droplet sizes, denoted as  $\sigma$ , ranged from a minimum of  $4.77 \mu\text{m}$  to a maximum of  $12.47 \mu\text{m}$ . When  $\sigma$  was at its minimum, the droplet sizes were primarily concentrated within three distinct bars in the range of 10 to  $25 \mu\text{m}$ . (as seen in Figure 6b). Conversely, when  $\sigma$  was at its maximum, the droplet sizes were dispersed over nine distinct bars, covering a broader span from 5 to  $60 \mu\text{m}$  (as seen in Figure 6a). Therefore, even within such a short icing event, the variability in the DSD in the air is substantial. The maximum standard deviation of droplet sizes is nearly three times that of the minimum standard deviation, highlighting the significant changes in DSD during this relatively brief period.

### 3.2 | Analytical model

According to Equation (1), a system of equations can be written like Equation (13) with known rates of ice accretion on IL1 and IL2,  $dM_1/dt$  and  $dM_2/dt$ , as well as the

diameters of the cylinders,  $d_1$  and  $d_2$ , and the wind speed  $U$  and ambient temperature  $T$  obtained from meteorological sensors. In this system of equations, only the MVD and the LWC ( $w$ ) are unknown. Although it is not possible to directly formulate  $f$ , numerical methods can be used to solve for the values of MVD and  $w$  as shown in Equation (14). Because the external shape of the cylinders after icing is not perfectly cylindrical, using Equation (2) to obtain the water droplet collision coefficient may introduce some errors into the calculations. However, these calculations can be partially validated by comparing the results with MVD and  $w$  measurements obtained from ICEMET.

$$\begin{cases} dM_1/dt = f(U, \text{MVD}, w, T, d_1) \\ dM_2/dt = f(U, \text{MVD}, w, T, d_2) \end{cases} \quad (13)$$

$$\begin{cases} \text{MVD} = F_1(dM_1/dt, dM_2/dt) \\ w = F_2(dM_1/dt, dM_2/dt) \end{cases} \quad (14)$$

As shown in Figure 7 in terms of the range of variation, both the calculated values of MVD and the measurements from ICEMET fall within the range of 10 to  $70 \mu\text{m}$ . However, the correspondence between the two is not good during the early period (9:30 a.m. to 12:00 p.m.), but after 12:00 p.m., both the trends and values become closer. Similarly, the comparative results for  $w$  also exhibit similar patterns. This is because the diameter of the IL2 cylindrical rod is  $57 \text{ mm}$ , which is larger than IL1, leading to a relatively smaller water droplet collision coefficient and slower ice accretion rate. As a result, the ice accumulation mass is close to zero during the early stages. In the calculation of Equation (14),  $dM_2/dt \approx 0$ ,

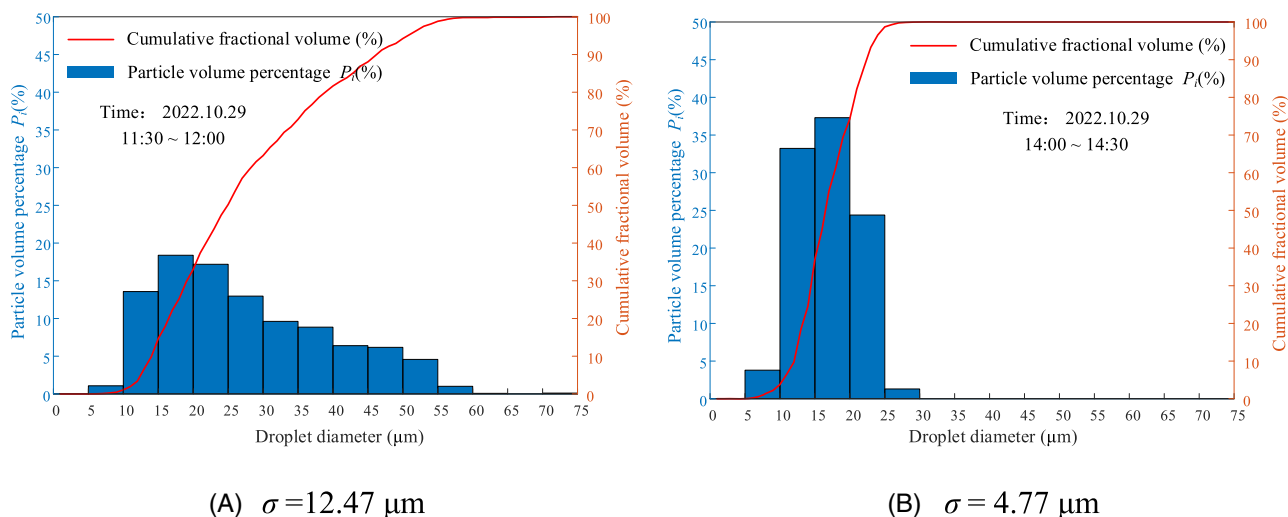


FIGURE 6 Water droplet size spectrum during the icing event. (a)  $\sigma = 12.47 \mu\text{m}$ . (b)  $\sigma = 4.77 \mu\text{m}$ .



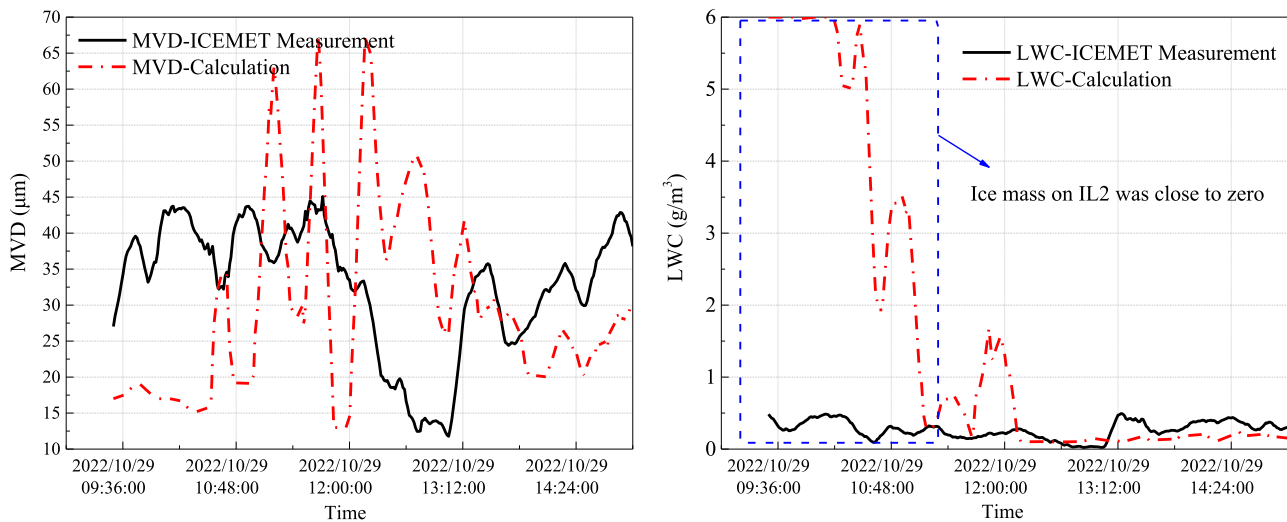


FIGURE 7 Comparison of MVD and  $w$  between ICEMET measurement and analytical calculations. MVD, median volume diameter.

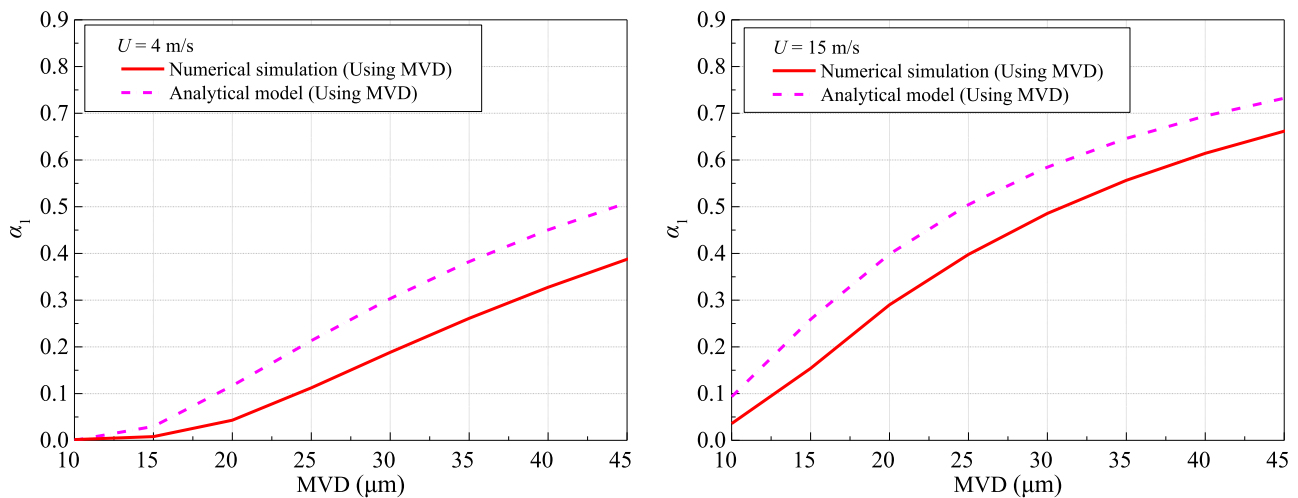


FIGURE 8 Collision efficiency  $\alpha_1$  calculation of 30 mm cylinder using MVD approach, analytical and numerical methods. MVD, median volume diameter.

which is equivalent to  $dM_2/dt$  being unknown, thereby causing a significant calculation error. As the ice accretion mass on IL2 gradually increases, the computed values of MVD and  $w$  show a good correspondence with ICEMET measurements. Because only the ice accumulation mass on two cylinders is used for the numerical solution of Equation (14), the solving process often falls into local optima, leading to significant discrepancies between the calculated and measured values. However, the overall trends of both are similar, making the calculated values a useful reference for comparison with ICEMET measurements.

As mentioned earlier, obtaining the water droplet collision coefficient for cylindrical bodies is a crucial step in icing simulations. Two methods that can be used include analytical models and numerical computational models

(CFD). However, it is not known whether there are significant differences in the results obtained from these two methods. Taking the 30 mm IL1 cylindrical body as an example, the collision efficiencies under different MVD were calculated using both methods under low wind speed (4 m/s) and high wind speed (15 m/s) conditions. The results are shown in Figure 8. From the calculation results, it can be observed that under both low and high wind speed conditions,  $\alpha_1$  increases nonlinearly with increasing MVD in both methods. However,  $\alpha_1$  from the analytical model is consistently greater than  $\alpha_1$  from the numerical computational model. If we consider  $\alpha_1$  from the numerical model as the accurate value, the  $\alpha_1$  from analytical model is consistently higher, with errors ranging from 0 to 0.12. When MVD is small (MVD  $\leq 15$   $\mu\text{m}$  at  $U = 4$  m/s, and MVD  $\leq 10$   $\mu\text{m}$  at

**TABLE 1** Water droplet size distribution spectrum measured using ICEMET sensor (October 29, 2022)

No	1	2	3	4	5	6	7	8	9	10	11
Start time	9:30	10:00	10:30	11:00	11:30	12:00	12:30	13:00	13:30	14:00	14:30
End time	10:00	10:30	11:00	11:30	12:00	12:30	13:00	13:30	14:00	14:30	15:00
$d_i$ ( $\mu\text{m}$ )	(DSD from ICEMET) Droplet size distribution-Particle Volume Percentage $P_i$ (%)										
5–10	0.00	0.00	0.00	0.61	1.07	0.00	3.79	0.00	0.00	0.00	0.00
10–15	0.00	0.00	5.04	7.47	13.57	3.46	33.23	0.00	0.00	0.00	0.00
15–20	0.30	0.00	7.81	8.40	18.39	13.50	37.30	3.44	2.06	0.53	4.00
20–25	13.14	11.52	7.98	5.11	17.19	32.10	24.38	6.71	35.40	6.29	14.09
25–30	38.57	7.14	7.56	5.36	12.97	21.80	1.30	34.23	43.50	32.81	19.77
30–35	19.25	9.78	13.50	28.82	9.62	16.60	0.00	37.32	10.60	42.07	17.57
35–40	16.08	28.17	23.60	29.44	8.85	9.73	0.00	16.37	7.39	15.66	19.54
40–45	7.95	28.86	19.40	10.48	6.40	2.80	0.00	1.93	1.05	2.64	17.39
45–50	4.71	7.71	8.33	4.31	6.18	0.00	0.00	0.00	0.00	0.00	5.38
50–55	0.00	6.76	6.71	0.00	5.77	0.00	0.00	0.00	0.00	0.00	2.26
MVD ( $\mu\text{m}$ )	31	39	38	35	25	25	17	31	26	32	34
$\sigma$ ( $\mu\text{m}$ )	7.62	10.20	11.43	9.83	12.47	7.04	4.36	5.53	4.87	4.77	8.71

$U = 15$  m/s), the error in the analytical model's  $\alpha_1$  is relatively small ( $\leq 0.05$ ). As MVD increases, this error remains around 0.1.

To further understand the differences in simulating ice accretion using MVD and DSD, the analytical model was selected to calculate the droplet collision efficiency  $\alpha_1$  of cylinder IL1 in the icing event. This calculation was performed using MVD, DSD ICEMET, and Langmuir B–I. The results are shown in Table 2. Due to the dynamic changes in the DSD (DSD ICEMET in Table 1) over 11-time intervals, the calculated  $\alpha_1$ , based on DSD ICEMET, varied between 0.295 and 0.574. If MVD is directly used to represent the DSD instead of DSD ICEMET in the calculation, the calculated  $\alpha_1$  ranged from 0.312 to 0.589, with a relative error varying between 0.2% and 14.6%. This implies that when simulating ice accretion, not considering the characteristics of the water DSD and using only MVD (DSD Langmuir A) for calculation can result in a maximum error of up to 14.6% in the calculation of  $\alpha_1$ . Furthermore, this significant error is not limited to specific cases; in interval nos. 3 and 4, the error value exceeded 14%.

To improve this situation, the Langmuir distribution B–I can be used to obtain a more accurate droplet collision coefficient  $\alpha_1$ . However, which Langmuir distribution that best approximates the real DSD ICEMET distribution is not constant. In the 11 intervals considered, three intervals obtained the closest  $\alpha_1$  using MVD, four intervals using Langmuir B, two intervals using Langmuir D, and two intervals using Langmuir I. When the most appropriate Langmuir distribution is

used, the maximum error in  $\alpha_1$  calculation always remains below 5%. Based on the aforementioned conclusions, when only the MVD of water droplets in the air is available, and specific characteristics of DSD are not, one can simultaneously employ Langmuir distributions B to I to perform supplementary calculations for  $\alpha_1$ . This enables an assessment of the potential error range associated with utilizing MVD for icing simulations. This is due to the fact that among Langmuir distributions B to I, there is always one that closely approximates the actual water DSD with an error of only  $\pm 5\%$ .

### 3.3 | Numerical simulations

Using time-varying environmental parameters such as wind speed, temperature, and LWC as inputs, the multiphase numerical simulations are carried out using MVD and droplet distribution spectrum. The resultant accreted ice mass is calculated using both, and results are compared with the experimental and analytical models. Analysis is carried out using cylinders with 30 mm diameters. The numerical simulations model provided more insight about air flow and droplet behavior. In order to compare the differences between the numerical model and the analytical model, the analytical model was replaced by the numerical model (CFD). Similarly, calculations for  $\alpha_1$  were performed with inputs of MVD, DSD ICEMET, and Langmuir B to I, following the methods outlined in Equations (8) to (9), and the results are presented in Table 3.

Irrespective of the water DSD used, the numerical model consistently yielded lower values for  $\alpha_1$  compared to the analytical model, with an absolute error of approximately 0.1. Furthermore, when comparing  $\alpha_1$ , the Langmuir distribution that best approximated DSD ICEMET also differed. In the results presented in Table 2, out of the 11-time intervals, nine had Langmuir distributions within the Langmuir A to D range as the closest

approximation to DSD ICEMET. However, in the results presented in Table 3, only three intervals fell within the Langmuir A to D range, with the remaining eight intervals falling within the Langmuir F to I range. Because the numerical computational model exhibits higher accuracy than the analytical model, and in terms of droplet size dispersion, Langmuir F to I surpass Langmuir A to D, it can be concluded that the results from the

**TABLE 2** Droplet collision coefficient  $\alpha_1$  obtained using different droplet size distribution in analytical model (October 29, 2022).

No	1	2	3	4	5	6	7	8	9	10	11
Start time	9:30	10:00	10:30	11:00	11:30	12:00	12:30	13:00	13:30	14:00	14:30
End time	10:00	10:30	11:00	11:30	12:00	12:30	13:00	13:30	14:00	14:30	15:00
Wind velocity (m/s)	7.3	8.1	8.1	9.7	12.4	14.0	14.5	14.2	13.2	12.0	10.7
MVD ( $\mu\text{m}$ )	31	39	38	35	25	25	17	31	26	32	34
Droplet size distribution	Droplet collision coefficient $\alpha_1$										
DSD ICEMET	0.450	0.553	0.500	0.499	0.456	0.491	0.295	0.574	0.504	0.553	0.547
MVD/Langmuir A	0.455	0.584	0.573	0.569	0.466	0.490	0.312	0.589	0.497	0.571	0.575
DSD Langmuir B	0.444	0.570	0.559	0.556	0.454	0.479	0.307	0.575	0.485	0.558	0.562
DSD Langmuir C	0.439	0.560	0.549	0.546	0.449	0.472	0.308	0.565	0.478	0.548	0.552
DSD Langmuir D	0.435	0.550	0.540	0.537	0.444	0.466	0.313	0.555	0.472	0.539	0.542
DSD Langmuir E	0.433	0.541	0.531	0.529	0.442	0.463	0.319	0.546	0.468	0.531	0.534
DSD Langmuir F	0.433	0.534	0.525	0.523	0.441	0.460	0.327	0.539	0.466	0.525	0.528
DSD Langmuir G	0.433	0.528	0.520	0.517	0.441	0.459	0.335	0.533	0.464	0.519	0.522
DSD Langmuir H	0.435	0.523	0.515	0.513	0.442	0.458	0.343	0.527	0.462	0.514	0.517
DSD Langmuir I	0.439	0.516	0.509	0.507	0.445	0.459	0.357	0.520	0.464	0.508	0.511

**TABLE 3** Droplet collision coefficient  $\alpha_1$  obtained using different droplet size distributions in numerical simulation (October 29, 2022).

No	1	2	3	4	5	6	7	8	9	10	11
Start time	9:30	10:00	10:30	11:00	11:30	12:00	12:30	13:00	13:30	14:00	14:30
End time	10:00	10:30	11:00	11:30	12:00	12:30	13:00	13:30	14:00	14:30	15:00
Wind velocity (m/s)	7.3	8.1	8.1	9.7	12.4	14.0	14.5	14.2	13.2	12.0	10.7
MVD ( $\mu\text{m}$ )	31	39	38	35	25	25	17	31	26	32	34
Droplet size distribution	Droplet collision coefficient $\alpha_1$										
DSD ICEMET	0.338	0.449	0.399	0.402	0.361	0.387	0.198	0.474	0.399	0.450	0.446
MVD/Langmuir A	0.341	0.479	0.468	0.467	0.355	0.381	0.205	0.488	0.388	0.468	0.472
DSD Langmuir B	0.335	0.468	0.456	0.455	0.348	0.374	0.206	0.477	0.379	0.457	0.462
DSD Langmuir C	0.334	0.462	0.451	0.451	0.348	0.374	0.215	0.472	0.378	0.452	0.456
DSD Langmuir D	0.340	0.457	0.447	0.446	0.351	0.374	0.225	0.467	0.380	0.448	0.452
DSD Langmuir E	0.345	0.456	0.445	0.446	0.357	0.378	0.238	0.464	0.382	0.447	0.451
DSD Langmuir F	0.350	0.455	0.445	0.444	0.360	0.378	0.252	0.462	0.382	0.446	0.451
DSD Langmuir G	0.358	0.451	0.444	0.442	0.367	0.385	0.260	0.462	0.389	0.444	0.449
DSD Langmuir H	0.367	0.455	0.446	0.446	0.374	0.390	0.276	0.461	0.395	0.447	0.450
DSD Langmuir I	0.376	0.458	0.451	0.451	0.387	0.407	0.302	0.463	0.404	0.450	0.453

numerical model more effectively reflect the dispersed characteristics of water droplet collision efficiency across different particle sizes. In icing simulations, using DSDs like Langmuir F-I with higher droplet size dispersion may be closer to the actual water DSD characteristics.

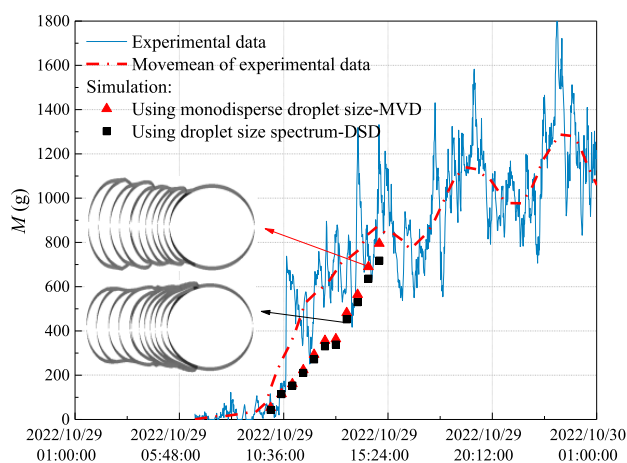
After obtaining accurate water droplet collision coefficients using MVD and DSD ICEMET as inputs, the numerical calculation model was used to further simulate the icing mass on the cylinder IL1, with input data shown in Table 4 and simulation results shown in Figure 9.

In terms of the final icing mass, the simulation using MVD produced 795 g, which was closer to the real value of 816 g, while the simulation using DSD yielded 717 g with a higher relative error. In fact, as expected, calculations using DSD parameters that are closer to the actual conditions should yield icing mass results that are closer to the real values. However, the results are quite the opposite. Several possible reasons for this discrepancy are hypothesized. (1) In this icing event, the higher wind speed resulted in a lesser

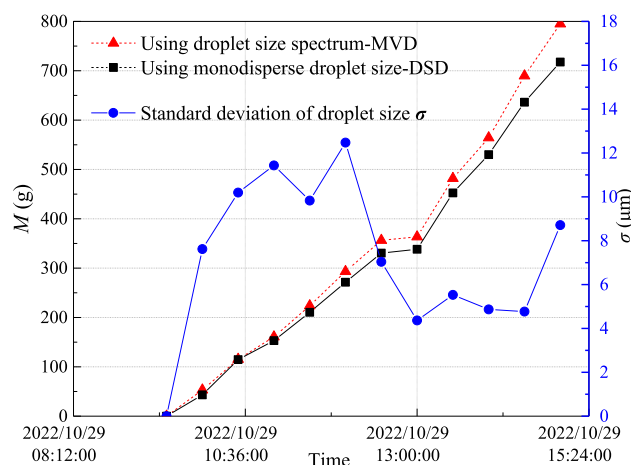
influence of water droplet collision rates by droplet size. (2) In contrast to MVD, DSD is better suited to represent the icing results of small and large water droplets on the cylinders, while the smaller droplets primarily collide with the sides of the cylinder's windward face. Due to the omission of factors such as icing roughness in the simulation, the process failed to faithfully depict the smaller droplets that should have collided with and frozen on both sides of the cylinder's windward face. Consequently, this led to a lower ice accumulation when simulated using DSD. Hence, this does not imply that using MVD is the better choice. As depicted in Figure 6a, in comparison to the icing patterns simulated using MVD, those obtained using DSD exhibit a broader distribution on the windward surface of the cylinder. With an increase in the number of iteration steps, the icing layer's distribution gradually narrows, which aligns with the observed icing patterns in the experiments. Conversely, the icing patterns obtained using MVD exhibit an opposite trend in terms of change over iterations. These simulation results are

TABLE 4 Numerical simulation input data (October 29, 2022).

Start time	9:30	10:00	10:30	11:00	11:30	12:00	12:30	13:00	13:30	14:00	14:30
End time	10:00	10:30	11:00	11:30	12:00	12:30	13:00	13:30	14:00	14:30	15:00
Wind velocity (m/s)	7.3	8.1	8.1	9.7	12.4	14.0	14.5	14.2	13.2	12.0	10.7
MVD ( $\mu\text{m}$ )	31	39	38	35	25	25	17	31	26	32	34
LWC ( $\text{g}/\text{m}^3$ )	0.34	0.40	0.21	0.24	0.18	0.20	0.04	0.36	0.27	0.39	0.31
Temperature ( $^{\circ}\text{C}$ )	-2.2	-2.1	-2.1	-2.1	-2.1	-2.3	-2.5	-2.9	-3.0	-3.7	-4.1



(A) Comparison of simulation and experimental  $M$



(B) Comparison of icing mass and  $\sigma$

FIGURE 9 Numerical simulation results of ice load. (a) Comparison of simulation and experimental  $M$ . (b) Comparison of icing mass and  $\sigma$ .



consistent with the earlier conclusions drawn from the Langmuir droplet distribution simulations, providing insights into the impact of using DSD and MVD on icing simulation results to some extent. In addition, it is undeniable that there are differences between the simulated and measured values, primarily due to two reasons: (1) The experiment was conducted under natural icing conditions, where the influence of wind caused significant fluctuations in the ice mass monitoring data on the cylinder surfaces, leading to some measurement errors. (2) To avoid excessive computational load, the environmental parameters used in the simulation, such as wind speed, were averaged over each time step, which also introduces some error and limits the accuracy of simulating time-varying turbulent flows in real environments.

## 4 | CONCLUSION

Following are the main findings of this study.

- In the calculation of the water droplet collision coefficient, the analytical model is primarily useful for quickly obtaining the overall water droplet collision efficiency on the surface of the cylinder, while the numerical calculation model can specifically reflect the differential local water droplet collision efficiency on the surface of the cylinder. As for the overall collision coefficient  $\alpha_1$  of the 30 mm-diameter cylinder IL1, under both low and high wind speed conditions,  $\alpha_1$  increases nonlinearly with increasing MVD in both methods. However,  $\alpha_1$  from the analytical model is consistently greater than  $\alpha_1$  from the numerical computational model, with errors ranging from 0 to 0.12. When MVD is small, the error in the analytical model's  $\alpha_1$  is relatively small ( $\leq 0.05$ ). As MVD increases, this error remains around 0.1.
- The field test results show that the icing rates of IL1 and IL2 (diameter of 30 mm and 57 mm) are different. At the beginning of icing, the ice accretion on IL1 is relatively faster, but gradually slower than IL2. Using the difference in icing rates of IL1 and IL2 to calculate MVD and *LWC*, the results show that when the icing mass on IL2 is small, the calculated MVD and *LWC* are significantly different from the ICEMET measurements. As the icing mass on IL2 increases, the calculation error decreases, and the calculated values become closer to the measurements.
- Based on the ISO-12494 analytical model, if MVD is directly used to represent the DSD instead of DSD

ICEMET in the calculation, the calculated  $\alpha_1$  has a relative error varying between 0.2% and 14.6%. This implies that when simulating ice accretion, not considering the characteristics of the water DSD and using only MVD (DSD Langmuir A) can result in a maximum error of up to 14.6% in the calculation of  $\alpha_1$ . When the most appropriate Langmuir distribution is used, the maximum error in  $\alpha_1$  calculation always remains below 5%.

- Compared with analytical model, the  $\alpha_1$  results from the numerical model more effectively reflect the dispersed characteristics of water droplet collision efficiency across different particle sizes. In icing simulations, using DSDs like Langmuir F-I with higher droplet size dispersion may be closer to the actual water DSD characteristics.
- In comparison to the icing shapes simulated using MVD, those obtained using DSD exhibit a broader ice distribution on the windward surface of the cylinder. With an increase in the number of iteration steps, the icing layer's distribution gradually narrows, which aligns with the observed icing shapes in the experiments. Conversely, the icing shapes obtained using MVD exhibit an opposite trend in terms of change over iterations.

## AUTHOR CONTRIBUTIONS

**Xingbo Han:** Methodology; software; validation; writing – original draft. **Muhammad Virk:** Writing – review and editing; supervision. **Hamza Asif:** Resources. **Anssi Mäkynen:** Resources. **Harri Juttula:** Resources. **Eero Molkoselkä:** Supervision. **Ville A. Kaikkonen:** Resources; data curation.

## ACKNOWLEDGEMENTS

The work reported in this paper is supported by the nICE project of UiT and Research Council of Norway (Project no- 324156). Special thanks to the research team of Oulu University for providing ICEMET sensor.

## CONFLICT OF INTEREST STATEMENT

The authors declare no conflicts of interest.

## DATA AVAILABILITY STATEMENT

The data that support the findings of this study are available on request from the corresponding author. The data are not publicly available due to privacy or ethical restrictions.

## ORCID

Xingbo Han  <https://orcid.org/0009-0006-3919-4991>

## REFERENCES

- ANSYS. (2021) Ansys FENSAP-ICE User Manual.
- Brun, B.R.J. & Mergler, H.W. (1953) Impingement of water droplets on a cylinder in an incompressible flow field and evaluation of rotating multicylinder method for measurement of droplet-size distribution, volume-median droplet size, and liquid-water content in clouds.
- Burnet, F. & Brenguier, J.L. (1999) Validation of droplet spectra and liquid water content measurements. *Physics and Chemistry of the Earth, Part B: Hydrology, Oceans and Atmosphere*, 24(3), 249–254.
- Charneski, M.D., Gaibrois, G.L. & Whitney, B.F. (1982) Flashover tests of artificially iced insulators. *IEEE Power Engineering Review*, PER-2(8), 17–18.
- Chuang, P.Y., Saw, E.W., Small, J.D., Shaw, R.A., Sipperley, C.M., Payne, G.A. et al. (2008) Airborne phase Doppler interferometry for cloud microphysical measurements. *Aerosol Science and Technology*, 42(8), 685–703.
- Dai, H., Zhang, J., Gui, H., Shen, L., Wei, X., Xie, Z. et al. (2022) Characteristics of aerosol size distribution and liquid water content under ambient RH conditions in Beijing. *Atmospheric Environment*, 291, 119397.
- Dhar, S. & Khawaja, H.A. (2021) Recognizing potential of LiDAR for comprehensive measurement of sea spray flux for improving the prediction of marine icing in cold conditions - a review. *Ocean Engineering*, 223, 108668.
- Dhar, S., Naseri, M., Khawaja, H.A., Samuelsen, E.M., Edvardsen, K. & Barabady, J. (2024) Sea-spray measurement tools and technique employed in marine icing field expeditions: a critical literature review and assessment using CFD simulations. *Cold Regions Science and Technology*, 217, 104029.
- Finstad, K.J., Lozowski, E.P. & Gates, E.M. (1988) A computational investigation of water droplet trajectories. *Journal of Atmospheric and Oceanic Technology*, 5(1), 160–170.
- Fugal, J.P., Shaw, R.A., Saw, E.W. & Sergeev, A.V. (2004) Airborne digital holographic system for cloud particle measurements. *Applied Optics*, 43(32), 5987–5995.
- Ge, J., Liu, J., Gui, K. & Ye, L. (2022) Atmospheric icing measurement and online ice type recognition for aircraft utilizing optical fiber sensor and machine learning algorithms. *Measurement*, 205, 112215.
- Goldberg, P., Apelt, S., Spitzner, D., Boucher, R., Mehner, E., Stöcker, H. et al. (2018) Icing temperature measurements of water on pyroelectric single crystals: impact of experimental methods on the degree of supercooling. *Cold Regions Science and Technology*, 151, 53–63.
- Gui, K., Liu, J., Ge, J., Li, H. & Ye, L. (2022) Atmospheric icing process measurement utilizing impedance spectroscopy and thin film structure. *Measurement*, 202, 111851.
- Guo, X., Wang, Z., Zhao, R., Wu, Y., Wu, X. & Yi, X. (2023) Liquid water content measurement with SEA multi-element sensor in CARDC icing wind tunnel: calibration and performance. *Applied Thermal Engineering*, 235, 121255.
- Hu, J., Lan, B., Xu, K., Jiang, X., Zhang, Z., Shi, B. et al. (2016) Artificial icing and AC flashover tests on glass insulators with silicone acrylate resin hydrophobic coatings. *IEEE Transactions on Dielectrics and Electrical Insulation*, 23(2), 1038–1047.
- Inoue, J. & Sato, K. (2023) Comparison of the depolarization measurement capability of a lidar ceilometer with cloud particle sensor sondes: a case study of liquid water clouds. *Polar Science*, 35, 100911.
- ISO 12494:2001(E). (2001) *Atmospheric icing of structures*. Geneva, CH: International Organization for Standardization.
- Jiang, X., Dong, B., Chao, Y., Zhang, Z., Hu, Q., Hu, J. et al. (2014) Diameter correction coefficient of ice thickness on conductors at natural ice observation stations. *IET Generation Transmission and Distribution*, 8(1), 11–16.
- Juttula, H.J., Kaikkonen, V.A., Molkoselka, E.O. & Makynen, A.J. (2022) Compensation of aerodynamic sampling effects of a cloud droplet instrument. *IEEE Access*, 10, 38813–38820.
- Kaikkonen, V.A., Molkoselkä, E.O. & Mäkynen, A.J. (2020) A rotating holographic imager for stationary cloud droplet and ice crystal measurements. *Optical Review*, 27(2), 205–216.
- Knezevicil, D. & Kindf, R.J. (2014) Determination of median volume diameter (MVD) and liquid water content (LWC) by multiple rotating cylinders.
- Lawson, R.P. & Blyth, A.M. (1998) A comparison of optical measurements of liquid water content and drop size distribution in adiabatic regions of Florida cumuli. *Atmospheric Research*, 47-48, 671–690.
- Lei, Y., Meng, Z., Jiang, X., Hu, J. & Zhang, Z. (2016) DC ice-melting and temperature variation of optical fibre for ice-covered overhead ground wire. *IET Generation, Transmission & Distribution*, 10(2), 352–358.
- Matsuda, H., Komuro, H. & Takasu, K. (1991) Withstand voltage characteristics of insulator string covered with snow or ice. *IEEE Transactions on Power Delivery*, 6(3), 1243–1250.
- Molkoselka, E.O., Kaikkonen, V.A. & Makynen, A.J. (2021) Measuring atmospheric icing rate in mixed-phase clouds using filtered particle data. *IEEE Transactions on Instrumentation and Measurement*, 70, 1–8.
- Shu, L., Li, H., Hu, Q., Jiang, X., Qiu, G., He, G. et al. (2018) 3D numerical simulation of aerodynamic performance of iced contaminated wind turbine rotors. *Cold Regions Science and Technology*, 148, 50–62.
- Shu, L., Wang, S., Jiang, X., Hu, Q., Liang, J., Yin, P. et al. (2014) Modeling of AC flashover on ice-covered composite insulators with different shed configurations. *IEEE Transactions on Dielectrics and Electrical Insulation*, 21(6), 2642–2651.
- Silverman, B.A., Thompson, B.J. & Ward, J.H. (1964) A laser fog disdrometer. *Journal of Applied Meteorology (1962)*, 3(6), 792–801.
- Sokolov, P. & Virk, M.S. (2019) Droplet distribution spectrum effects on dry ice growth on cylinders. *Cold Regions Science and Technology*, 160, 80–88.
- Spirig, R., Vogt, R. & Feigenwinter, C. (2021) Droplet size distribution, liquid water content and water input of the seasonally variable, nocturnal fog in the central Namib Desert. *Atmospheric Research*, 262, 105765.
- Tiitta, P., Leskinen, A., Kaikkonen, V.A., Molkoselkä, E.O., Mäkynen, A.J., Joutsensaari, J. et al. (2022) Intercomparison of holographic imaging and single-particle forward light scattering in situ measurements of liquid clouds in changing atmospheric conditions. *Atmospheric Measurement Techniques*, 15(9), 2993–3009.

- Volat, C., Farzaneh, M. & Mhaguen, N. (2011) Improved FEM models of one- and two-arcs to predict AC critical flashover voltage of ice-covered insulators. *IEEE Transactions on Dielectrics and Electrical Insulation*, 18(2), 393–400.
- Wang, W., Pazmany, A., Lei, H., Chen, C., Nie, H. & Zuo, D. (2023) Measurement of supercooled liquid water path in cold clouds based on a 183GHz airborne microwave radiometer. *Atmospheric Research*, 285, 106655.
- Zhang, J., Makkonen, L. & He, Q. (2017) A 2D numerical study on the effect of conductor shape on icing collision efficiency. *Cold Regions Science and Technology*, 143, 52–58.

**How to cite this article:** Han, X., Virk, M., Asif, H., Mäkynen, A., Juttula, H., Molkoselkä, E., & Kaikkonen, V. A. (2024). Atmospheric icing meteorological parameter study using field experiments and simulation. *Meteorological Applications*, 31(6), e70013. <https://doi.org/10.1002/met.70013>